

Processing-microstructure relationships in compocast magnesium/SiC

V. LAURENT, P. JARRY, G. REGAZZONI
Péchiney, Centre de Recherches de Voreppe, France

D. APELIAN
College of Engineering, Worcester Polytechnic Institute, Worcester, MA, USA

Compocasting experiments were conducted to investigate the feasibility of the process as applied to the AZ91D magnesium alloy–SiC particles system. Processing–macro/microstructure relationships were examined. Three temperature–time processing sequences were investigated: stirring temperature maintained above liquidus; stirring temperature in the semi-solid temperature range; and lastly, an imposed temperature rise above the liquidus after stirring in the mushy zone. Stirring temperature and particle size significantly affect spatial particle distribution and porosity level. The easy incorporation and even dispersion of particles in the matrix suggest good wetting of SiC particles by the magnesium matrix. Impact fracture surfaces show strong bonding at the particle/matrix interface. A reaction takes place at the matrix/particle interface whilst stirring at temperatures above the liquidus. Reaction products have been identified. Finally, the mechanical properties of a compocast ingot which was extruded have been studied and are reported. This work clearly points out that there is a preferred procedure to follow during compocasting to obtain an optimum microstructure. The procedure is to add the reinforcing materials to the semi-solid alloy followed by stirring above the liquidus temperature.

1. Introduction

Metal matrix composites (MMC) are of great interest because of their improved mechanical properties over monolithic systems. In particular, metal matrix composites have high specific strength and stiffness [1–3]. However, the manufacturing cost of composites is still high, primarily due to the processing costs, whether it be diffusion bonding, powder metallurgy, squeeze casting, etc., and to the initial cost of the reinforcement. Among the processes investigated, the compocasting process has been shown to be an effective processing scheme with acceptable economics. The process, as it was first described by Mehrabian *et al.* [4], consists of entrapping the reinforcement phase in a highly viscous, semi-solid alloy. The reinforcement phase is entrapped by the thixotropic semi-solid aggregates which are created when the melt is vigorously agitated during the early phases of solidification. The particles are then expected to develop a true interface with the matrix, resulting in their retention [5]. An alternative approach is the vortex method [6, 7], where the reinforcement phase is introduced into the melt which is not in a semi-solid state.

Magnesium-based alloys are attractive matrices because of their low density (35% lighter than aluminium) and high strength-to-weight ratios. Moreover, rheocasting has been successfully applied to magnesium alloys [8]. In this investigation, the AZ91D alloy was selected, the reinforcement phase being SiC

particles. The latter was chosen for its hardness and its relative stability with magnesium compared to Al_2O_3 particles [9–13].

The objectives of this study were to: (i) evaluate the feasibility of producing Mg–SiC composites by both the compocasting process and the vortex method; (ii) establish the processing–macro/microstructure relationships, specifically, distribution of the reinforcement phase and porosity in the cast component as a function of content and size of the reinforcement phase, stirring temperature and other processing parameters; (iii) characterize the chemistry and strength of the particle/matrix interface; (iv) evaluate the mechanical properties of Mg–SiC compocast material subsequent to extrusion.

2. Background

Compocasting as a process to produce aluminium matrix composites has been studied and has received attention over recent years [14–20]. Recent work has shown that the incorporation of SiC particles into the magnesium matrix has improved specific stiffness and strength properties compared to the monolithic alloy and also elevated temperature fatigue strength, creep and wear resistance [21, 22]. However, the process presents some quality-related difficulties: the particles may be unevenly distributed and a high level of porosity may exist [23–25]. With regard to the dispersion of

the second-phase particles, the uniformity of distribution is influenced by processing variables such as the mixing system used and processing conditions such as stirring speed, stirring temperature and time [6, 26, 27]. In addition, density differences between matrix and reinforcement phase, size and shape of the particles, apparent viscosity of the mixture, etc., have a predominant influence on the particle distribution [16, 17]. Porosity in the compocast product, is commonly attributed to gas entrapment [6, 7, 24].

In recent years, alternative processes and approaches have been reported which address the defects in particle distribution and porosity in compocast magnesium-based alloys. In one of them [27], a compact of SiC particles was infiltrated with molten magnesium; the Mg-SiC charge was then remelted and stirred, similar to the compocasting scheme. Another approach used magnetohydrodynamic stirring [22]. Post-compocasting sequences, such as squeeze casting, die casting or extrusion, have been performed to yield improved microstructures.

However, the influence of the processing variables on defect evolution and understanding of the origins of defects during solidification have not been thoroughly investigated. This is a prerequisite and of paramount importance; if compocasting is commercially adopted to manufacture ingots and near-net shaped components, the control of defects (and their elimination) must be well understood. The focus of this study is to provide this understanding.

3. Experimental procedure

3.1. Materials

The AZ91D alloy was selected for the compocasting experiments because of its wide melting range (468–596 °C). Such a wide range enables one to vary

easily and to control the solid fraction during solidification for isothermal holding and stirring during compocasting. Table I shows the alloy composition; the Al-Mg binary phase diagram along with the relationship of the solid fraction as a function of temperature, is given by Fig. 1. The reinforcement particles are high-purity SiC (99.5% SiC, 0.3% SiO₂, 0.07% C, 0.01% Si, Fe, Al, Ca). Two average sizes of SiC particles were used: grit-size 240 (average 54 μm) and grit-size 800 (average 12 μm). Prior to introducing the SiC particles into the slurry, they were dried in a furnace at 400 °C for a period of 18 h at a pressure of 20 mm Hg.

3.2. Apparatus

The rheocasting apparatus used in this study has been previously described [8], and is shown in Fig. 2. The steel crucible containing the metal and the stainless steel impeller were coated with boron nitride. The charge of about 1 kg was melted under a flow of argon of ultra-high purity; the temperature of the melt was monitored with a K-type thermocouple dipped into the melt. Once stirring was completed, the furnace was lowered and the whole steel chamber was water quenched. The impeller rotated in the 200–650 r.p.m. speed range; the stirring speed was controlled by a stroboscope.

In order to feed the second-phase particles into the chamber, a powder feed unit was connected to the furnace; it allowed the control of the feeding rate through a difference of pressure, after calibration. The particles were fluidized by an air vibrator and carried into the chamber by a flow of argon of ultra-high purity (99.999%, O₂ < 1 p.p.m., H₂ < 1 p.p.m., H₂O < 1 p.p.m.). The carrier gas was also used to protect the surface of the melt from oxidation. A

TABLE I Nominal composition wt % of AZ91D alloy

Mg	Al	Zn	Mn	Si	Cu	Ni	Fe	Other impurities
bal.	8.5–9.5	0.5–0.9	≥ 0.15	≤ 0.02	≤ 0.015	≤ 0.001	≤ 0.005	≤ 0.01

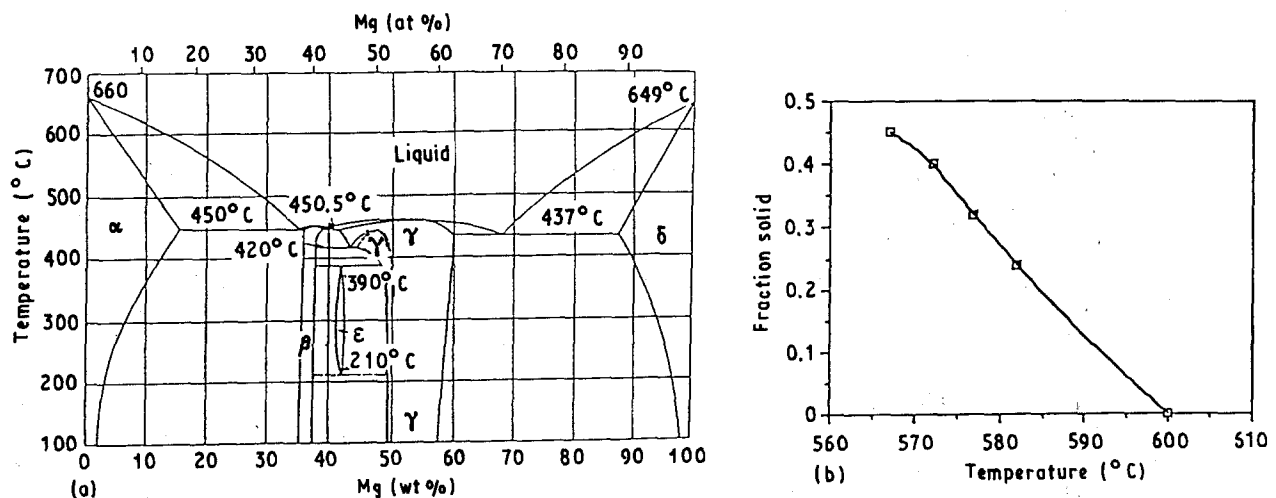


Figure 1 The Al-Mg system: (a) phase diagram; (b) solid fraction as a function of temperature, Al-9% Mg binary alloy [8].

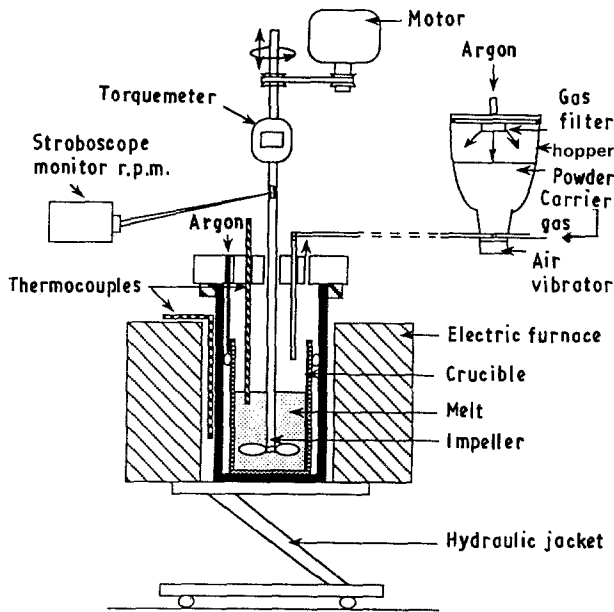


Figure 2 Schematic drawing of the experimental apparatus used for compocasting experiments.

torquemeter was attached to the shaft to control the shear stresses applied to the composite slurry.

3.3. Methods

Fig. 3 shows the temperature-time curve indicating the trajectory and the temperature excursions used in these experiments. As pointed out in Fig. 3, there are different phases of the processing scheme.

Phase 1: melting of the charge.

Phase 2: the melt is brought to the stirring temperature. The stirring temperature may be above the liquidus temperature, such as $T_{\text{liquid}+}$, or in the semi-solid range such as shown in Fig. 3 as T_{ss} . The stirring temperature will be noted in the text as T^* whether the stirring temperature is above the liquidus or in the semi-solid range.

Phase 3: the reinforcement phase is introduced into the melt or slurry.

Phase 4: from the temperature $T_{\text{liquid}+}$ or T_{ss} , the composite may be directly quenched to room temperature or it may be remelted to a temperature above the liquidus, T_{max} , prior to quenching.

Essentially, three different stirring temperature, T^* , sequences were evaluated (see Fig. 3)

Sequence A: the matrix is totally in the liquid state at $T_{\text{liquid}+}$, where $T_{\text{liquid}+} > T_{\text{liquidus}}$.

Sequence B: the matrix is partially frozen in the semi-solid temperature range at T_{ss} where $T_{\text{liquidus}} > T_{\text{ss}} > T_{\text{solidus}}$.

Sequence C: Sequence B is followed by remelting of the metal matrix prior to quenching.

In order to establish the processing-macro/micro-structure relationships, experiments were conducted for different processing conditions as shown in Table II. Table II indicates the average size of the SiC particles, the volume per cent of the particles introduced, the temperature, time and speed of stirring. The total fraction solid given in Table II is the total fraction of the reinforcement phase, as well as the solid

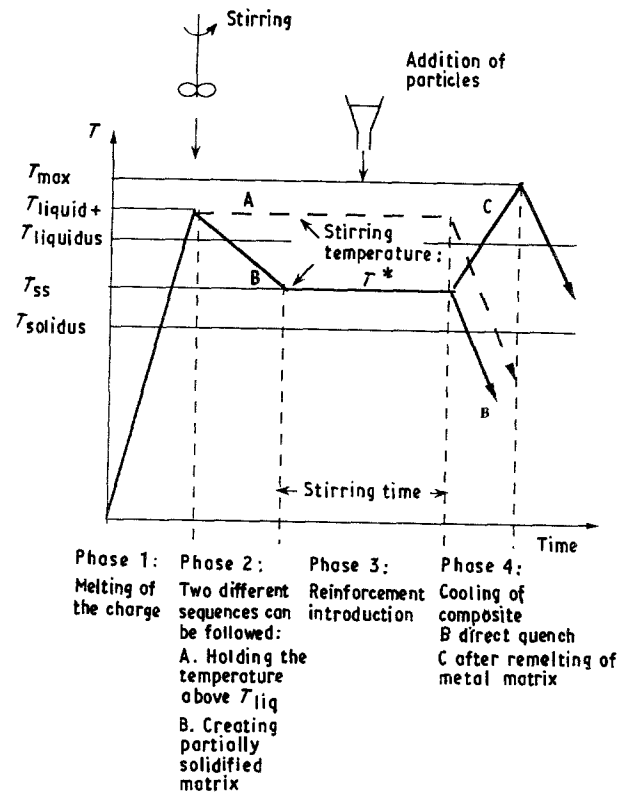


Figure 3 Schematic representation of the temperature-time sequences for the compocast process.

fraction of the base metal present at the injection stage. Variation of the solid fraction of the base metal as a function of temperature is estimated using the Scheil equation [28] and the Mg-Al binary phase diagram, Fig. 1.

3.4. Analysis

The macrodistribution of particles throughout the composite ingot was investigated by radiography and metallographic examination of various sections from the compocast ingots. Metallographic examination and image analysis were conducted to characterize the microdistribution of particles and to evaluate the porosity content. Area porosity values are reported as the average of the analysis of nine frames performed on representative regions of the compocast ingot.

The particle/matrix interface was characterized by SEM analysis of fractured and polished surfaces. The phases in the matrix and their repartition in relation to SiC particles were also analysed by SEM. X-ray diffraction analysis was used to identify the phases present as well as the reaction products after dissolution of the matrix. Mechanical properties of the compocast ingots were evaluated subsequent to extrusion.

4. Results

The feasibility of compocasting to produce magnesium-based composites containing SiC particles was confirmed: the incorporation of SiC particles in the magnesium matrix was successful in all the experimental conditions explored - see Table II. Particle incorporation was achieved even in a fully liquid matrix; in contrast to aluminium, magnesium wets

TABLE II Matrix of compositing experiments

Run	SiC particles		Stirring T^* (°C)	f_s^a	$f_s^{T^*b}$	Stirring speed (r.p.m.)	Stirring time (min)		
	Size (μm)	vol %							
1	54	15	689 \pm 3	0.0	0.15	620 \pm 10	45		
2			637 \pm 2	0.0	0.15	620 \pm 10	45		
3			620 \pm 3	0.0	0.15	620 \pm 5	90		
4			620 \pm 5	0.0	0.15	620 \pm 5	25		
5			581 \pm 3	0.30	0.30	620 \pm 10	50		
			588 \pm 1	0.19	0.33				
6			574 \pm 3	0.40	0.40	560 \pm 5	45		
			582 \pm 2	0.28	0.43				
7			581 \pm 1	0.30	0.30	575 \pm 5	90		
			587 \pm 2	0.20	0.35				
8			581 \pm 1	0.30	0.30	600 \pm 5	60		
			585 \pm 2	0.24	0.39				
9			574 \pm 2	0.40	0.40	365 \pm 5	35		
			587 \pm 1	0.20	0.35				
			/595 ^b	0.03	0.18		10		
10			575 \pm 5	0.39	0.39	620 \pm 5	45		
			586 \pm 1	0.22	0.37				
	/616 ^b	0.0	0.15		15 (5 above liquidus)				
11		25	607 \pm 2	0.0	0.25	622 \pm 3	60		
12	12	15	574 \pm 2	0.40	0.40	630 \pm 10	45		
			584 \pm 2	0.25	0.40				
13			572 \pm 2	0.42	0.42	615 \pm 5	45		
			584 \pm 1	0.25	0.40				
			/616 ^b	0.0	0.15		22 (5 above liquidus)		
14			610 \pm 5	0.0	0.15	620 \pm 5	45		
15			575 \pm 1	0.39	0.39	360 \pm 5	45		
			585 \pm 1	0.24	0.39				
			/622 ^b	0.0	0.15		16 (10 above liquidus)		
16			575 \pm 2	0.39	0.39	625 \pm 5	75		
			588 \pm 1	0.19	0.34				
			/616 ^b	0.0	0.15		16 (10 above liquidus)		
17				25	585 \pm 5	0.24	0.24	625 \pm 5	45
					591 \pm 3	0.12	0.37		

^a f_s is the fraction solid of Mg-9 wt % Al alloy as evaluated using the Scheil equation (see Fig. 1b).

^b $f_s^{T^*}$ is the total fraction of the reinforcement phase as well as the fraction solid of the base metal, f_s , when holding and stirring the slurry at T^* .

^cThe symbol “/” stands for the increase in temperature up to the specified temperature before quench.

SiC well and is a better “host” for particle embedment. Infiltration difficulties in aluminium alloys with respect to SiC are quite well documented [14]. Adding magnesium to the aluminium base melt has been found to facilitate SiC wetting [29]; this certainly is in line with the results of this investigation.

4.1. Macro/microstructure of the composite

Cross-sections of ingots showing the macrodistribution of SiC particles in the magnesium matrix for both sizes of particles, 12 and 54 μm , and for Sequences A, B and C are seen in Fig. 4. In Fig. 4a corresponding to Sequence A and large SiC particles, one can note that

the upper section of the ingot contains a region which resembles oxide sludge on top of a typical melt. The foam displays an abundance of macropores surrounded with carbide particles. Under the foam layer, a matrix layer free of particles results from a limited settling effect. When the reinforcing phase is added to the matrix in the semi-solid temperature range (Sequences B and C) the macrodistribution is quite homogeneous: only a very limited foam layer is found and no evidence of settling, see Fig. 4b. The smaller SiC particles yield a uniform and homogeneous distribution irrespective of the processing sequence applied, Fig. 4c and d. It should be noted that Sequence A resulted in a significant fraction of porosity in the bulk composite as shown in Fig. 4c.

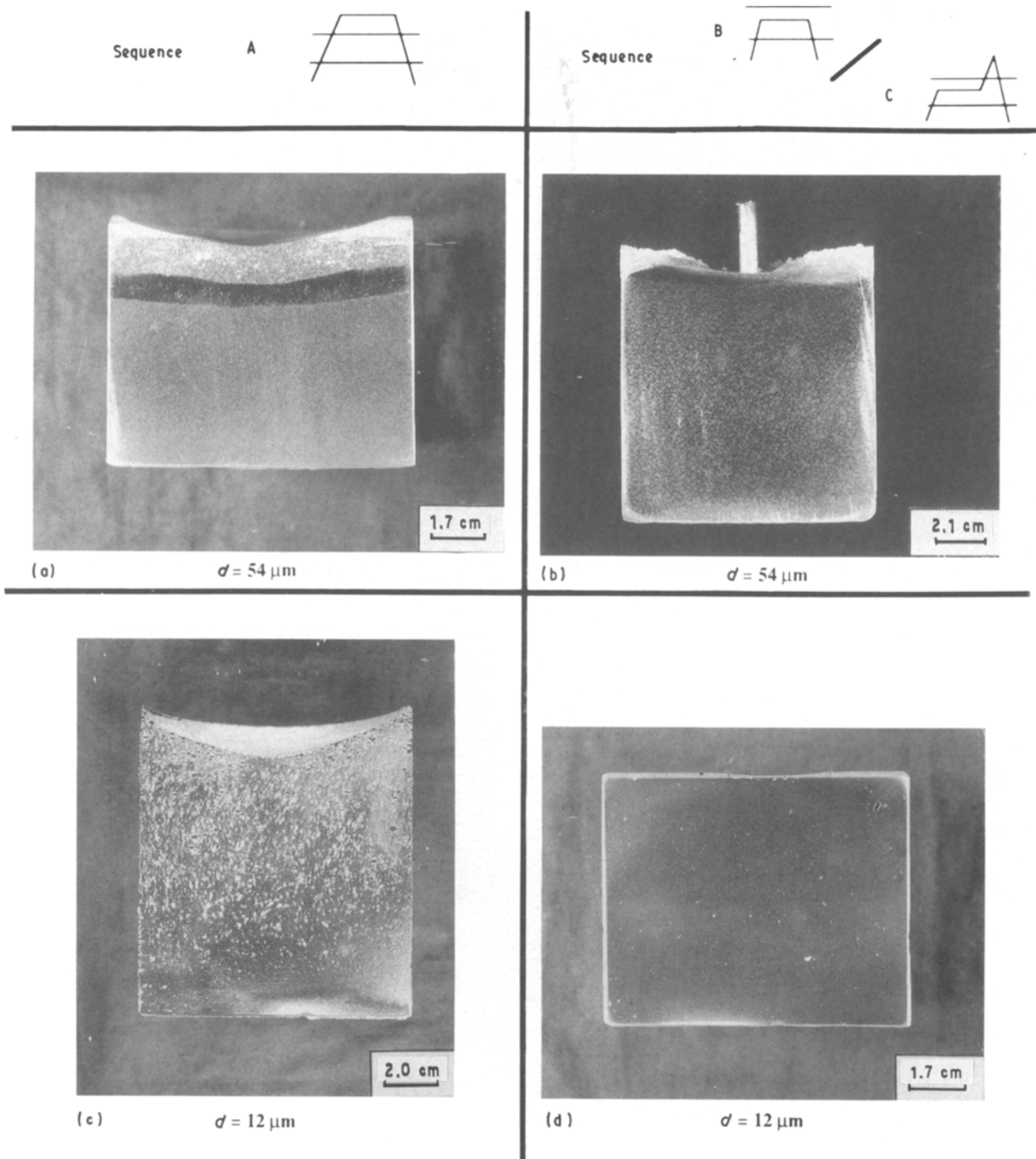


Figure 4 Effect of temperature sequence on macrodistribution of SiC particles in ingots: (a) $T^* = 607^\circ\text{C}$ (Run 11), Sequence A, particles of $54\ \mu\text{m}$ size; (b) $T^* = 581\text{--}587^\circ\text{C}$ (Run 7), Sequence B, particles of $54\ \mu\text{m}$ size; (c) $T^* = 610^\circ\text{C}$ (Run 14), Sequence A, particles of $12\ \mu\text{m}$ size; (d) $T^* = 572\text{--}584 + /616^\circ\text{C}$ (Run 13), Sequence C, particles of $12\ \mu\text{m}$ size.

The settling of $54\ \mu\text{m}$ sized particles was shown to depend strongly on the position of the impeller relative to the slurry height. Raising the impeller by 1 cm in the mixture of about 10 cm height resulted in settling of the particles in the lower half part of the ingot when stirring above the liquidus. Even a short excursion above the liquidus (Sequence C) was found sufficient to allow extensive settling, as shown in Fig. 5. Note the sharp transition between the reinforced and unreinforced parts of the ingot. When the stirring temperature was in the semi-solid temperature range (Sequence B), only a restricted settling effect was found with the same "high" position of the impeller.

In the following section, the effects of the processing variables during compocasting on both porosity and microdistribution of the particles in the compocast component are presented. Microdistribution of the reinforcement phase and porosity are mainly affected by the stirring temperature, the amount and size of the second phase, and the position of the impeller.

The effects of the three temperature sequences, A, B and C, on porosity and particle microdistribution in composites reinforced with $54\ \mu\text{m}$ sized SiC particles are illustrated in Fig. 6. Fig. 6a and b show micrographs of composites where the particles were added to the molten matrix at 689°C (Sequence A) and to the

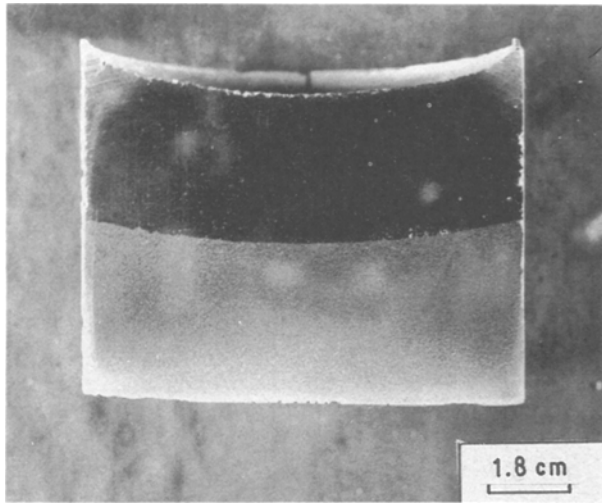


Figure 5 Effect of T^* and position of impeller on macrodistribution of SiC particles in ingots: $T^* = 575\text{--}586 + /616^\circ\text{C}$ (Run 10), Sequence C, particles of $54\ \mu\text{m}$ size, impeller in a high position.

semi-solid alloy at $584 \pm 4^\circ\text{C}$ (Sequence B), respectively. In Fig. 6a the particles are agglomerated in small aggregates of few particles and engulfed by the magnesium matrix during solidification. The presence of many pores appearing as black spots is also evident in the micrograph. In Fig. 6b, the distribution of particles is quite different in that they are located within the intercellular regions, the cells being the non-dendritic primary islands. SiC particles have been pushed into these intercellular regions while mixing in the semi-solid alloy. The porosity content of the latter is reduced compared to the former, Fig. 6b versus Fig. 6a. As previously mentioned, the large second-phase particles settle at the bottom of the casting at temperatures above the liquidus when the impeller is in a high position. The micrograph of Fig. 6c shows the bottom part of the ingot in the case of Sequence C. The particles are highly concentrated but still separated by the matrix. The porosity content of the reinforced part of the ingot was found to be quite low.

When considering the micrographs of $12\ \mu\text{m}$ sized SiC particles composites (Fig. 7), the amount of porosity noted is overwhelming. The highest porosity content was found when the particles were stirred in the molten metal: a porosity content as high as 34% was evaluated when the composite was held at 610°C (Sequence A). Remelting the metal matrix after stirring in the semi-solid temperature range (Sequence C) has the potential to reduce porosity; however, these trials were not reproducible and further work is needed.

A similar trend with respect to the microdistribution of SiC particles as a function of stirring temperature T^* , was seen with both 12 and $54\ \mu\text{m}$ sized SiC reinforcement phase. The amount of solid fraction present during stirring greatly influences the distribution of the SiC particles: the larger the solid fraction present in the slurry, the more isolated are the pockets where the SiC particles are located. However, increasing for a short while the temperature above liquidus after stirring in the mushy zone (Sequence C) was sufficient to dissolve the primary cells and to disperse the second-phase particles. The final distribution of

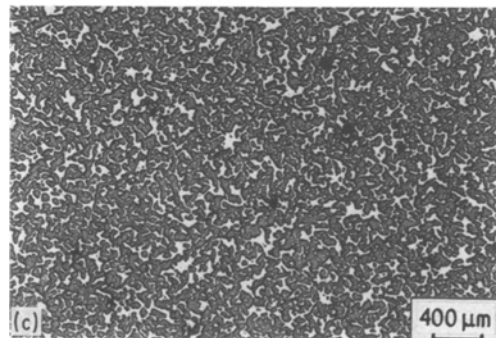
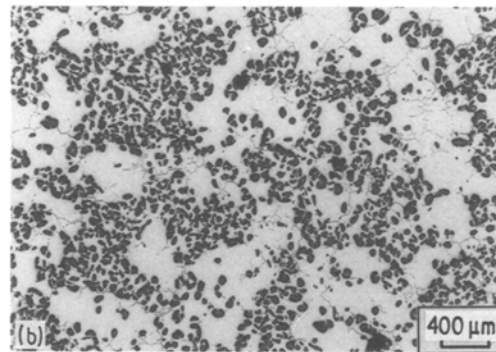
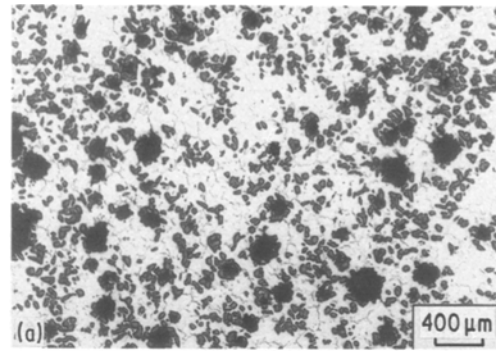


Figure 6 Effect of T^* on the microstructure of AZ91D + 15 vol % SiC particles ($54\ \mu\text{m}$ size): (a) $T^* = 689^\circ\text{C}$ (Run 1), Sequence A; (b) $T^* = 581\text{--}588^\circ\text{C}$ (Run 5), Sequence B; (c) $T^* = 575\text{--}586 + /616^\circ\text{C}$ (Run 10), Sequence C, after settling, impeller in a high position.

particles was found not to be affected by the prior thermal excursion in the mushy zone (see Fig. 7c). When increasing the SiC content from 15 vol % to 25 vol % in the semi-solid slurry, the primary cells get finer and their morphology changes as seen in Fig. 7d by the development of arms around the cells.

Fig. 8 shows the amount of porosity as a function of stirring temperature, particle size and particle content. When large particles are added to the stirred alloy, the increase in porosity content is closely related to the increase in stirring temperature (Fig. 8a). No clear relationship is found with small particles; the amount of porosity is roughly increased by one order of magnitude when the particle size decreases from $54\ \mu\text{m}$ to $12\ \mu\text{m}$ (see Fig. 8b). The particle content has a direct effect on the observed porosity in the compocast components (see Fig. 8b). It is interesting to note, however, that reheating the semi-solid slurry above the liquidus (Sequence C) does not result in an increase of the porosity content (Fig. 8a).

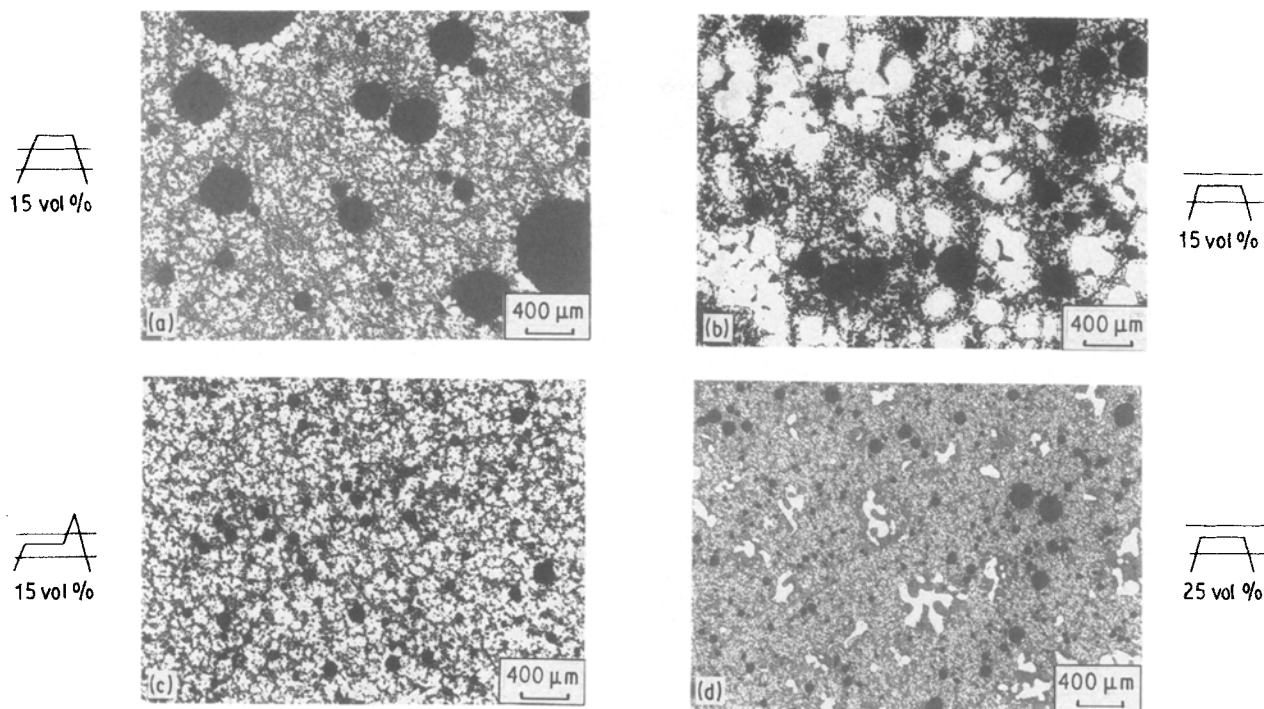


Figure 7 Effect of T^* on the microstructure of AZ91D + SiC particles (12 μm size): (a) $T^* = 610^\circ\text{C}$ (Run 14), Sequence A, 15 vol %; (b) $T^* = 574\text{--}584^\circ\text{C}$ (Run 12), Sequence B, 15 vol %; (c) $T^* = 572\text{--}584 + /616^\circ\text{C}$ (Run 13), Sequence C, 15 vol %; (d) $T^* = 585\text{--}591^\circ\text{C}$ (Run 17), Sequence B, 25 vol %.

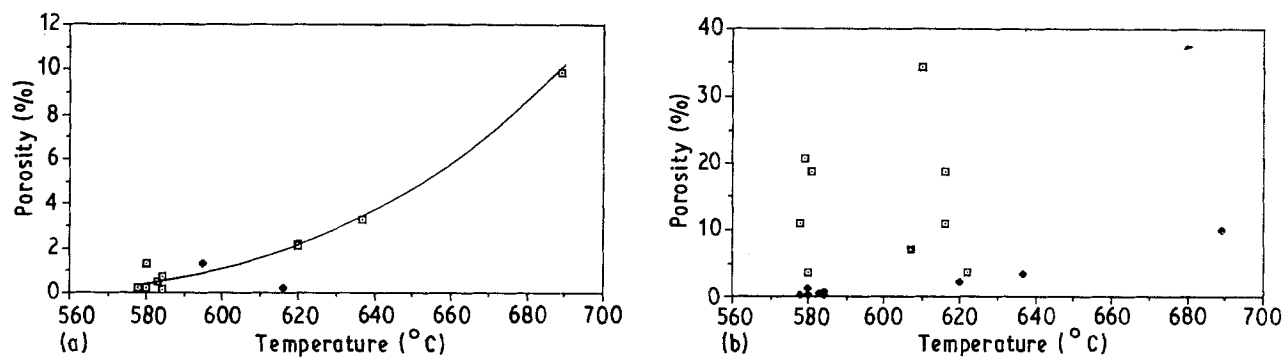


Figure 8 Effect of stirring temperature, T^* , particle content and particle size on porosity content in Mg/SiC composites. (a) Effect of T^* on porosity (%) with 54 μm sized particles, (\square) 15 vol %, (\blacklozenge) 15 vol %, reheating the semi-solid slurry above the liquidus; (b) Effects of T^* and vol % SiC on porosity (%) with both sizes of particles: 54 μm (\blacklozenge) 15 vol %, (\blacksquare) 25 vol %; (\square) 12 μm , 15 vol %.

The micrographs of Fig. 9 exhibit the topology of various microdefects found in the compocast composites. Agglomeration of small SiC particles closely surrounding a primary cell of the matrix, as seen in Fig. 9a, was commonly revealed in metallographic samples of composites reinforced with 25 vol % 12 μm sized particles. Fig. 9b and c show the pore morphology: the pores are generally spherical and always associated with SiC particles irrespective of particle size. In addition, impingement and coalescence of pores were observed, as seen in Fig. 9b.

Metallurgical aspects of the microstructure are illustrated by Fig. 10. Fig. 10a shows a scanning electron micrograph where the SiC particles (15 vol %) are pushed within the intercellular regions ($T^* = 584 \pm 4^\circ\text{C}$, Sequence B). The white areas were identified to be the aluminium-rich component $\text{Mg}_{17}\text{Al}_{12}$ of the eutectic phase by X-ray diffraction analysis. Fig. 10b shows another scanning electron micrograph of the composite at a higher magnification where the 54 μm

sized reinforcement phase was introduced at 689°C . Once again, the white region is the aluminium-rich component $\text{Mg}_{17}\text{Al}_{12}$ of the eutectic phase. The grey sharp-edged particles in the upper left of the micrograph are large crystals of Mg_2Si produced in significant amounts when stirring at the higher temperatures. Note the presence of small black particles at the particle/matrix interface; the nature of these particles was investigated and is discussed in the following section. Fig. 10c shows 12 μm sized SiC particles within the magnesium metal matrix. The effect of finer SiC particles on the morphology of the eutectic phase, i.e. its refinement, can be noted in Fig. 10c in contrast to Fig. 10b.

Effects of processing variables on macro/microdistribution of particles and porosity content are summarized in Table III. Before giving further results, one may conclude from the foregoing that Sequence C is the procedure which produces the soundest and most homogeneously reinforced composite; Sequence C

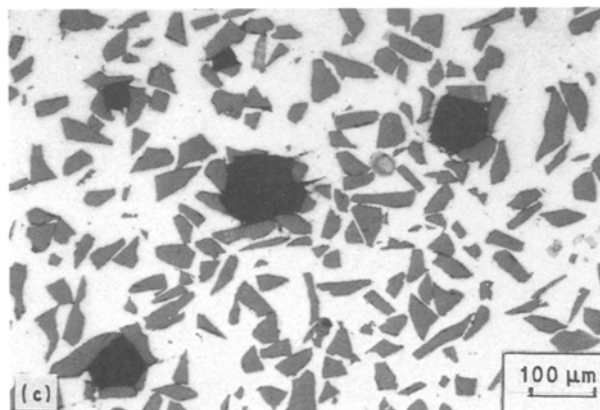
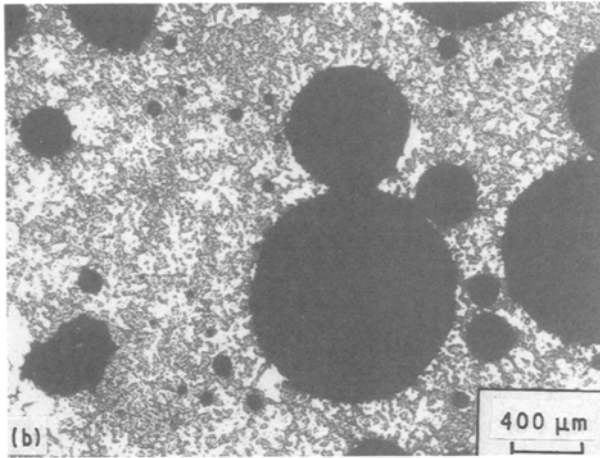
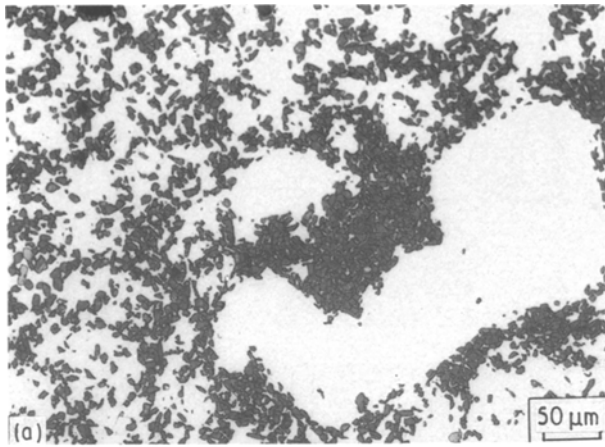


Figure 9 Morphology of defects found in AZ91D composites reinforced with SiC particles. (a) Agglomeration of small SiC particles around solid matrix globules ($T^* = 585\text{--}591^\circ\text{C}$, Sequence B, 25 vol % SiC particles of $12\ \mu\text{m}$ size). (b) Coalescence of gas bubbles ($T^* = 610^\circ\text{C}$, Sequence A, 15 vol % SiC particles of $12\ \mu\text{m}$ size). (c) Attachment of SiC particles of $54\ \mu\text{m}$ size on gas bubbles.

has been found to eliminate segregation of particles formed while stirring in the mushy zone without increasing the amount of porosity.

4.2. Nature of the particle/matrix interface

The properties of the SiC/Mg alloy interface are quite important because it is the interface which will ultimately control the ensuing mechanical properties. The adhesion at the particle/matrix interface can be

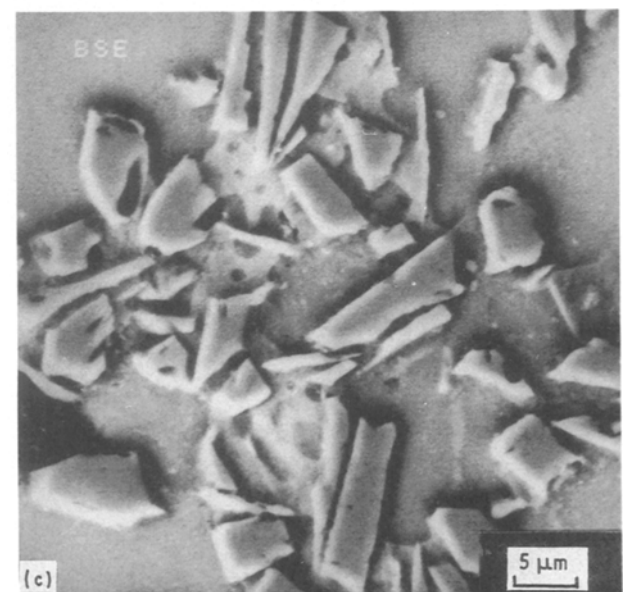
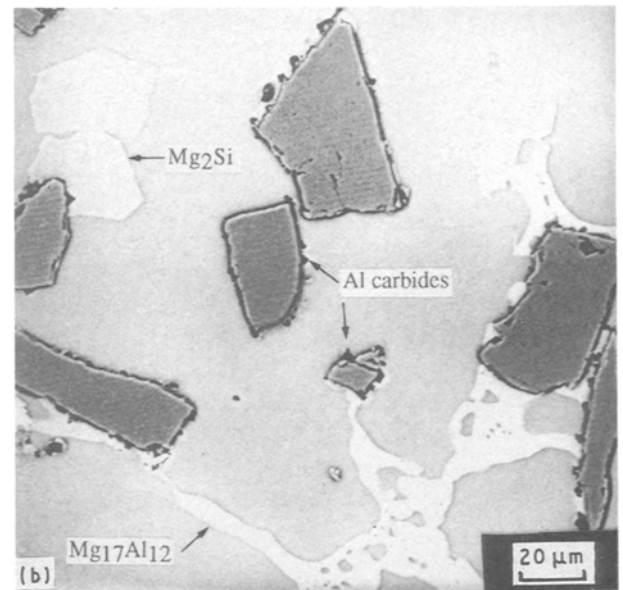
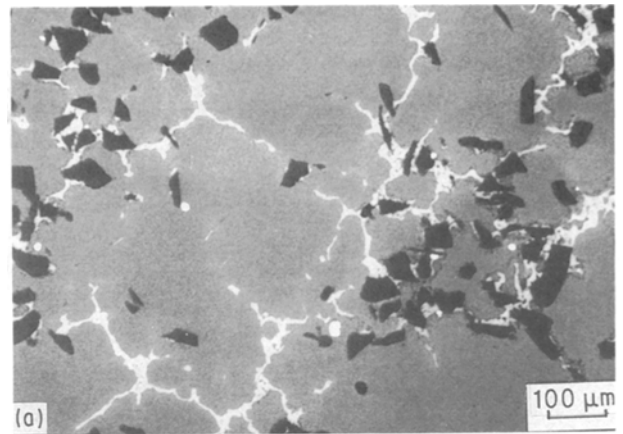


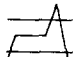


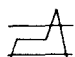


Figure 10 Metallurgical aspects of the composite microstructure. (a) Back-scattered electron micrograph showing rosette-like primary phase (grey), $\text{Mg}_{17}\text{Al}_{12}$ phase (bright) and SiC particles (black). ($T^* = 581\text{--}588^\circ\text{C}$, Sequence B, 15 vol % SiC particles of $54\ \mu\text{m}$ size.) (b) Back-scattered electron micrograph showing $\text{Mg}_{17}\text{Al}_{12}$ (bright), Mg_2Si crystals (light grey, in the upper-left side), SiC particles (dark grey) and reaction product at the Mg/SiC interface (black). ($T^* = 689^\circ\text{C}$, Sequence A, 15 vol % SiC particles of $54\ \mu\text{m}$ size.) (c) Back-scattered electron micrograph showing fine $\text{Mg}_{17}\text{Al}_{12}$ phase surrounding SiC particles of $12\ \mu\text{m}$ size. ($T^* = 575\text{--}588 + /616^\circ\text{C}$, Sequence C, 15 vol % SiC particles.)

TABLE III Settling effect, microdistribution of particles and porosity content as a function of particle size, temperature sequence, impeller position

Particle size (μm)	Sequence	Impeller position ^a /settling effect	Microdistribution	Porosity content
54	A 	High/extended Low/restricted	Homogeneous	Increase with T
	B 	High/limited Low/no	Segregation of particles between cells of matrix	Low
	C 	High/extended Low/restricted	Homogeneous	Low
12	A 	No effect	Small clumps of particles underlining fine dendrites	Very high
	B 	No effect	Segregation of particles between globular cells of matrix	Scattered values (9–21%)
	C 	No effect	Small clumps of particles underlining fine dendrites	Scattered values (3.5–19%)

^aThe “high” position of impeller means raising 1 cm in comparison with the “low” position.

characterized through the metallographic examination of fracture surfaces. The micrograph of Fig. 11a shows the fracture surface of a composite where SiC particles of 54 μm were mixed with the magnesium alloy in the semi-solid temperature range (Sequence B). The micrograph reveals the absence of voids at the interface, suggesting a strong particle–matrix bond between particles and matrix.

Dimples in the matrix (seen in the upper left of the micrograph) and breakage of particles are evident, characteristic, respectively, of ductile failure in the matrix and brittle fracture of the reinforcing phase. This association results from the microscopic inhomogeneities observed in the composite stirred in the semi-solid state. No evidence of reaction product nor erosion of particle surface was given at the SiC/Mg matrix interface. The micrograph of Fig. 11b shows a polished section with clean SiC particles.

When a high stirring temperature was selected, i.e. $\sim 100^\circ\text{C}$ above the liquidus, a discontinuous layer of microcrystals at the SiC particle/matrix interface was found. These can be seen on fractured surfaces, see Fig. 11c, where small crystals 1–2 μm in size have adhered to the SiC particles. In the particular micrograph of Fig. 10c, the SiC particles are emerging in a microshrinkage. A companion micrograph of this situation is also shown in Fig. 11d where metallographic evidence of the eroded SiC particles is seen. SEM and X-ray diffraction analysis of the reaction product after dissolution of the matrix was carried out. The SEM analysis showed two peaks of aluminium and carbon and a small one of oxygen. The X-ray trace indicated the presence of the hexagonal SiC phase and a phase whose peaks did not fit with aluminium carbide. It is

postulated that a complex ternary Al–C–O phase is formed. In addition, numerous Mg_2Si crystals of large size were formed due to a reaction between magnesium and silicon subsequent to aluminium reduction of SiC, as shown in Figs 10b and 11d.

4.3. Mechanical properties

The tensile properties of extruded AZ91D and AZ91D–15 vol % SiC composite alloys are given in Table IV. Both reinforced and unreinforced alloys were stirred in the semi-solid temperature range prior to extrusion (Sequence B). For comparison purposes, room-temperature tensile test results for die-cast AZ91–SiC particle composites published by the Dow Chemical Company [14] are reported in Table IV. For the composite containing 15 vol % SiC particles (54 μm), the room-temperature yield strength (257 MPa), is 20% greater than that for unreinforced AZ91D (215 MPa), and the ultimate tensile strength (289 MPa) is very close to that for the unreinforced alloy (296 MPa). A significant improvement in elastic modulus (up to 46%) is also obtained; however, the total elongation of the composite is drastically decreased to 0.7% compared to the value of 10.2% measured for the unreinforced alloy. As expected, the microstructural features are elongated by the extrusion. Matrix cells form particles with depleted strips after extrusion (see Fig. 12). Some porosities are associated with the denser zones of the aligned particles. There is no reason not to believe that optimization of the extrusion process will contribute to healing defects and heterogeneities which account for the low ductilities observed.

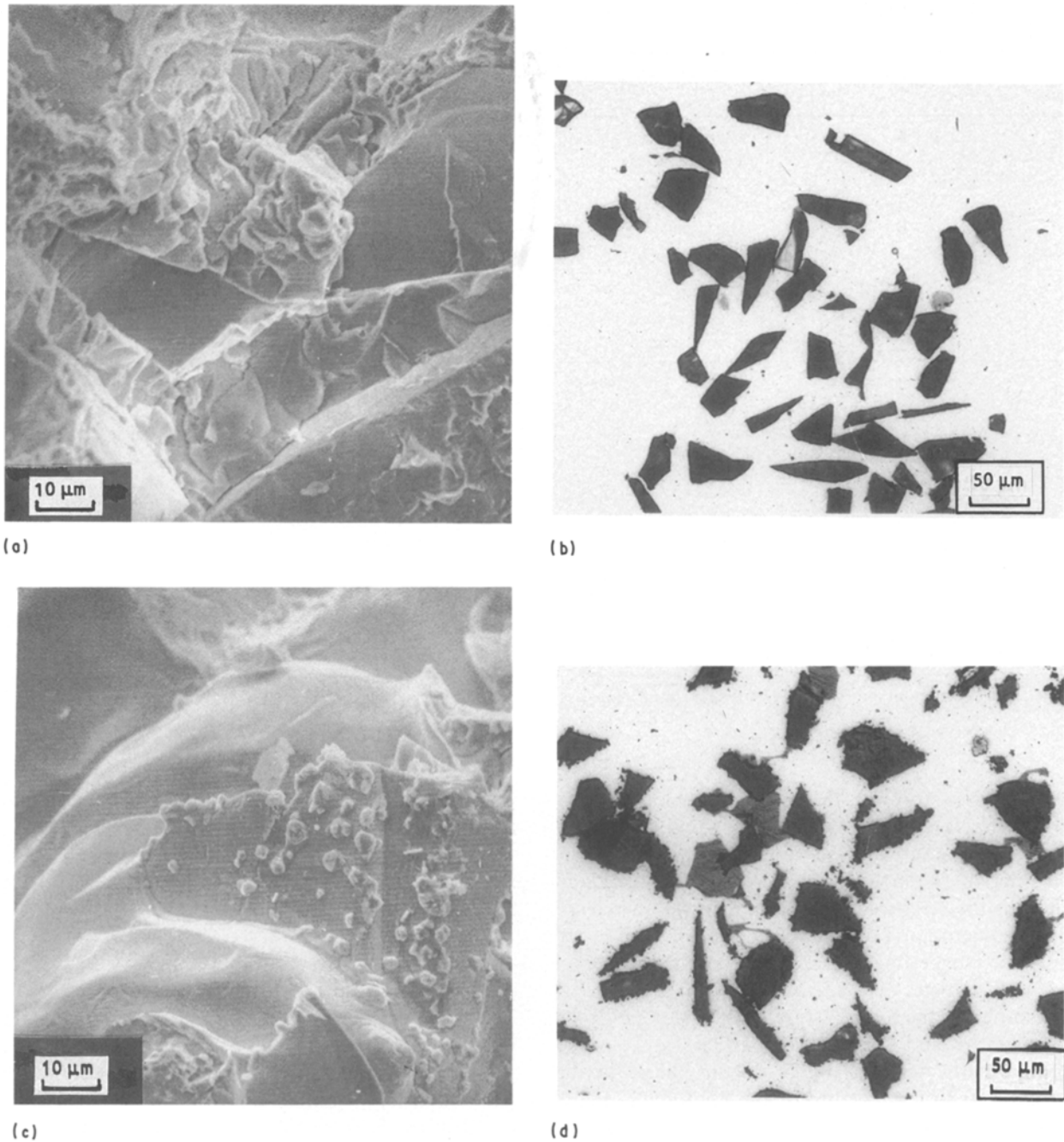


Figure 11 Effect of T^* on the particle/matrix interface. (a, b) $T^* = 581\text{--}588\text{ }^\circ\text{C}$, Sequence B, 15 vol % SiC. (a) Fracture surface showing breakage of particles and ductile fracture of matrix without formation of any void at the interface. (b) Polished surface: clean SiC particles. (c, d) $T^* = 689\text{ }^\circ\text{C}$, Sequence A, 15 vol % SiC. (c) Fracture surface: SiC particles emerging in a microshrinkage showing carbide microcrystals on their surfaces. (d) Polished surface: Mg_2Si phase associated with carbide microcrystals.

TABLE IV Tensile properties of extruded rheocast AZ91D as a function of SiC particle content

Material	Tensile yield strength (MPa)	Ultimate tensile strength (MPa)	Total elongation (%)	Elastic modulus (GPa)
AZ91D ^a	215	296	10.2	45
AZ91D + 15 vol % SiC ^b	257	289	0.7	64.5
AZ91 + 15 vol % SiC ^c	205	233	1.1	60.0

^a Values given in [8]; extrusion conditions: diameter ratio 20; temperature 250 °C; pressure 165 bar.

^b This work. The composite ingot tested was the one corresponding to Run 7, Sequence B. The extrusion conditions are similar to those in^a: diameter ratio 16; temperature 250 °C; pressure 165 bar.

^c Values given in [21]; the values are results of room-temperature tensile tests for die cast AZ91–SiC particles composites.

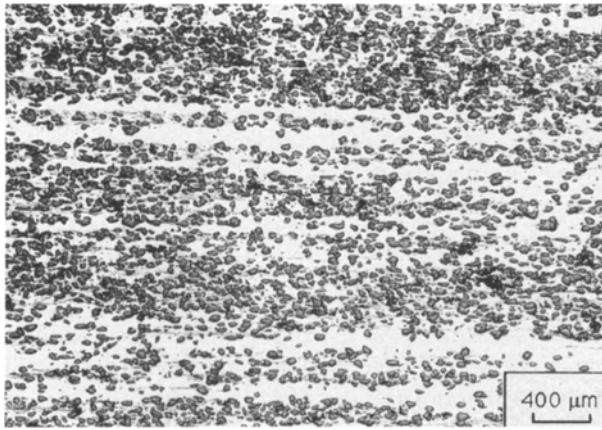


Figure 12 Microstructure of AZ91D + 15 vol % SiC particles (54 μm) after extrusion – see Table IV for extrusion conditions.

5. Discussion

The results presented raise issues pertaining to the effects of rheocasting processing conditions on the evolution of defects and heterogeneities in the compocast structure. In this section, the discussion is focused on two crucial microstructural features in compocast ingots: settling of the reinforced phase and porosity.

5.1. Settling

Settling occurred when large particles of 54 μm size were mixed to a fully molten matrix. The position of the impeller was shown to have a tremendous effect on settling. This can be explained through the rheology of the mixing system and the associated flow pattern [30]. The results suggest that the pumping axial flow is not strong enough to counteract the natural settling of the second-phase particles (the density of SiC is 3.2 g cm⁻³ compared with 1.65 g cm⁻³ for the matrix). The effect of the impeller position on settling is limited when stirring in the semi-solid state and is suppressed with small particles irrespective of the stirring temperature. The former can be explained by the high viscosity of the semi-solid slurry having a solid fraction in the 0.3–0.4 range which hinders settling. The insensitivity to particle size can be understood by Stoke's Law which relates the settling rate to the square diameter of the reinforcing phase.

5.2. Porosity

5.2.1. Porosity formation

A high porosity level is commonly found in particle-reinforced composites produced by compocasting. The defect is usually attributed to gas entrapment; two probable sources of gas are moisture, absorbed onto the particle surface, and atmosphere bubbles entrapped in the particle aggregates. Metal matrices like aluminium or magnesium alloys react with moisture to dissolve hydrogen. The local oversaturation of liquid metal in hydrogen may result in the nucleation and growth of gas bubbles. Stirring the melt under a flow of argon provides the second source of gas bub-

bles: gas is physically drawn into the melt by the vortex and forms bubbles to decrease its surface tension. The stirring can also nucleate gas bubbles in the region of low pressure immediately behind the blades of the impeller. Moreover, when imperfectly fluidized particles are added to the melt, atmosphere gas entrapped in clumps of particles prior to their addition are introduced into the melt.

These results do not allow one to conclude whether hydrogen or argon constitutes the primary source of gas bubbles. However, the results suggest the synergism of both gases in bubble formation through the following mechanism: suction of argon bubbles in the forced vortex, adhesion of particles on bubble surfaces and diffusion of hydrogen (dissolved in the melt or adsorbed at the particle surface) to bubbles.

5.2.2. Porosity retention and elimination

Once formed, the gas bubbles may be affected by different mechanisms. Owing to the stirring action, gas bubbles can grow by collision, coalescence, as well as due to mass-transfer of hydrogen. The micrograph in Fig. 9b illustrates the collision-coalescence mechanism of the gas bubbles in the melt mixed with small particles. During their motion, the bubbles will also impinge on SiC particles. Once collision occurs, the particles attach themselves to the bubbles via surface tension forces. The net change in free energy during attachment of SiC particles is

$$\Delta F = \sigma_{SV} - (\sigma_{SL} + \sigma_{LV}) \quad (1)$$

where σ_{SV} , σ_{SL} and σ_{LV} are the SiC/gas interfacial tension, SiC/Mg interfacial tension and Mg/gas interfacial tension, respectively. The three interfacial tensions are related to the contact angle, θ , by Young's equation

$$\sigma_{SV} = \sigma_{SL} + \sigma_{LV} \cos \theta \quad (2)$$

ΔF is then expressed as

$$\Delta F = \sigma_{LV}(\cos \theta - 1) \quad (3)$$

The net free energy change is negative as soon as the wetting is non-perfect ($\theta > 0^\circ$). However, the gain in energy will be more substantial when the particles are not wetted by the matrix ($\theta > 90^\circ$). Although a beneficial effect of magnesium addition on the wetting of ceramics by aluminium alloys has been reported, no quantitative information on the wetting of ceramics by magnesium is available in the literature. Good wetting of a covalent high-melting solid, such as SiC, by a metal is not expected unless a strong chemical reaction between the metal and ceramic exists [31]. The presence of silica on silicon carbide may well be at the origin of the improvement in wettability through the reaction with magnesium.

The adhesion of SiC particles to bubbles increases the stability of the "foam" formed by the gas bubbles dispersed in the metal. Without a layer of particles, the bubbles would float up to the top surface due to their low density. The terminal velocity is expressed as [32]

$$V = (8/3(\rho_m - \rho_b)rg/C_d)^{1/2} \quad (4)$$

where r is the radius of the bubble, ρ_m , ρ_b the density of molten magnesium alloy and bubbles, respectively, g the acceleration due to gravity, and C_d the drag coefficient. The attachment of particles will decrease the float-up rate because it increases the apparent density of the gas bubble and the viscous drag applied to the bubble. Different mechanisms for bubble elimination can be suggested. Inertial forces and viscous drag exerted by the stirred mixture (particles and matrix) on large particles will eventually overcome the surface tension effect and remove the particles from the bubbles. In addition, relatively large bubbles in motion are subjected to deformation and ultimately to fragmentation into smaller bubbles [33, 34]. Such a process is accelerated by the attachment of particles to the surface of the bubble which increases the interfacial viscosity or rigidity [35]. Both mechanisms (removal of particles from the bubbles and break-up of bubbles surrounded by particles) result from shear stresses applied by the flowing mixture of SiC particles and metal in the presence of gravity and centrifugal fields.

5.2.3. Practical means of decreasing the amount of porosity

Porosity may be reduced by inhibiting gas bubble formation, limiting gas bubble size and any means to eliminate gas bubbles.

5.2.3.1. Limiting gas introduction. The amount of gas introduced into the melt should be reduced by following specific experimental procedures. Hydrogen feeding of the mixture can be decreased by an effective treatment of the particles: drying the fluidized particles under vacuum above 400 °C without further exposure to air. The smaller the particles, the more critical the treatment because the surface to volume ratio increases with decreasing size.

To limit argon bubble suction, one may preferentially stir in the semi-solid temperature range because the high viscosity of the semi-solid slurry reduces vortexing and turbulent flow in the region of the agitator and consequently gas entrapment. Another way of limiting gas entrapment is to use anti-vortex baffles.

5.2.3.2. Limiting pore size. Stirring in the semi-solid temperature range should be a way of limiting the pore size. The process results in pushing particles and bubbles in-between primary cells of the matrix. Such particle segregation will enhance shear action on bubbles which will aid breakage into small bubbles, and removal of particles from the bubbles. The presence of matrix cells should also limit the growth of bubbles by impingement and coalescence mechanisms.

The effect of shear stress level on porosity may be at the origin of the sharp increase in pore size and content with small particles. Decreasing the particle size results in increasing the apparent viscosity at

constant weight per cent of particles [7, 36]. Such increase in viscosity may greatly affect the efficiency of the mixing system in developing shear action, as suggested in our work by the presence of both large gas bubbles and large solid matrix globules of complex shape in composites reinforced with small particles (see micrographs of Fig. 7).

5.2.3.3. Eliminating gas bubbles. Remelting the composite subsequent to stirring in the mushy zone is a means of partially eliminating bubbles. Mixing in the fully molten matrix promotes the floating-up motion of the bubbles and their retention in the foam layer as formed in the upper region of the composite ingots.

6. Conclusions

1. Magnesium matrix composites reinforced with SiC particles can be made by compocasting.

2. Particles can be introduced either in the liquid alloy or in the semi-solid alloy.

3. Particle distribution depends essentially on the stirring temperature. When stirring is done above the liquidus, uniform distribution is obtained but with an elevated level of porosity. When stirring is done within the melting range, SiC particles are located in between the primary matrix cells; the level of porosity is significantly reduced.

4. Porosity level is much higher with small particles.

5. Stirring the composite above the liquidus subsequent to addition of the reinforcement phase in the mushy alloy produces the soundest and most homogeneously reinforced composite.

6. The position of the impeller is an important parameter as far as settling of large particles is concerned because it affects the flow patterns of the melt/slurry.

7. In all the composites examined, an excellent interface between the SiC particles and the magnesium matrix was formed. However, when stirring at high temperatures, the formation of aluminium carbides at the interface and large Mg_2Si crystals are observed.

8. Tensile tests performed on extruded composites reveal a high level of modulus (up to 64.5 GPa compared to 45 GPa for magnesium), an improvement of 20% in yield strength and tensile strength equivalent to the unreinforced matrix. Ductility level is low, in relation to residual agglomerates of particles and associated porosity after extrusion.

Acknowledgements

The authors gratefully acknowledge the support provided by the P echiney Corporation. Thanks are due to J. Bouvaist and S. Bercovici, Pechiney, for having made possible a one year study at Professor Apelian's laboratory. Thanks are also due to R. Rey-Flandrin, Centre de Recherches de Voreppe, for his assistance.

References

1. D. E. HAMMOND, *Modern Casting* August (1989) 29.
2. D. M. SCHUSTER, M. D. SKIBO and W. R. HOOVER, *Light Metal Age* February (1989) 15.

3. P. ROHATGI, *Modern Casting* April (1988) 47.
4. R. MEHRABIAN, R. G. RIEK and M. C. FLEMINGS, *Metall. Trans.* **5A** (1974) 1899.
5. C. G. LEVI, C. J. ABBASCHIAN and R. MEHRABIAN, *ibid.* **9A** (1978) 697.
6. P. K. GHOSH, S. RAY and P. K. ROHATGI, *Trans. J. Inst. Metals* **25** (1984) 440.
7. M. D. SKIBO and D. M. SCHUSTER (Dural aluminium composites corporation). US Pat. C22C21/00, 1/09, 5 November 1987.
8. A. TISSIER, D. APELIAN and G. REGAZZONI, *J. Mater. Sci.* **25** (1990) 1184.
9. F. C. BENNETT, T. E. LEONTIS and S. L. COULING, in "Proceedings of the 34th Meeting of the International Magnesium Association" (International Magnesium Association, Ohio, 1977) p. 23.
10. K. SUGANUMA, T. OKAMOTO, T. HAYAMI, Y. OKU and N. SUZUKI, *J. Mater. Sci.* **23** (1988) 1317.
11. J. E. HACK, R. A. PAGE and R. SHERMAN, *Metall. Trans.* **16A** (1985) 2069.
12. Ernest Sung Chor Chin, Report No. AD-A179 912, US Army Materials Technology Laboratory, January 1987.
13. R. WARREN and C. H. ANDERSSON, *Composites* **15** (2) (1984) 106.
14. J. W. McCOY, C. JONES and F. E. WAWNER, *SAMPE Q.* January (1988) 37.
15. F. M. HOSKING, Report no. DE81028185, Sandia National Laboratories, July 1981.
16. F. A. GIROT, L. ALBRINGE, J. M. QUENISSET and R. NASLAIN, *J. Metals* November (1987) 18.
17. S. DAS, R. ASTHANA and P. K. ROHATGI, *Int. Met. Rev.* **31** (1986) 115.
18. T. Z. KATTAMIS and J. A. CORNIE, in "Proceedings of 1988 World Materials Congress", edited by S. C. Fishman and A. K. Dhingra (ASM International, Chicago, 1988) p. 47.
19. W. R. LOUE and W. H. KOOL, *ibid.* p. 327.
20. M. A. BAYOUMI and M. SUERY, *ibid.* p. 167.
21. B. A. MIKUCKI, S. O. SHOOK, W. E. MERCER and W. G. GREEN, in "Proceedings of 43rd Annual World Magnesium Conference", Los Angeles, 1986 (International Magnesium Association, Virginia, 1986) p. 13.
22. D. L. ALBRIGHT, *ibid.*, p. 33.
23. A. MORTENSEN, J. A. CORNIE and M. C. FLEMINGS, *J. Metals* **40** (1988) 12.
24. S. RAY, in "Proceedings of 1988 World Materials Congress" edited by S. C. Fishman and A. K. Dhingra (ASM International, Chicago, 1988) p. 77.
25. K. YAMADA, S. SEKIGUCHI and T. MATSUMIYA, in "Proceedings of 34th International SAMPE Symposium and Exhibition", Nevada 1989 (SAMPE, California, 1989).
26. W. P. JENSEN, S. M. and R. T. TALTON Jr, in "Proceedings of Symposium Series no. 10 AI.Ch.E.-I.Chem.E.", London 1965 (American Institute of Chemical Engineers, New York, 1965) p. 82.
27. E. M. KLIER, MS Thesis, Massachusetts Institute of Technology (1988).
28. D. B. SPENCER, R. MEHRABIAN and M. C. FLEMINGS, *Met. Trans.* **3A** (1973) 1925.
29. F. A. GIROT, L. ALBRINGE, J. M. QUENISSET and R. NASLAIN, *J. Metals* November (1987) 18.
30. S. NAGATA, "Mixing principles and applications" (Wiley, New York, 1975).
31. Ju. V. NAIDICH, *Progr. Surf. Membrane Sci.* **14** (1981) 353.
32. G. R. GEIGER and D. R. DOIRIER, "Transport Phenomena in Metallurgy" (Addison-Wesley, Mass. 1973).
33. F. D. RUMSCHEIDT and S. G. MASON, *J. Colloid Sci.* **16** (1961) 238.
34. R. CLIFT, J. R. GRACE and M. E. WEBER, "Bubbles, Drops and Particles" (Academic Press, New York, 1978).
35. H. J. KARAM and J. C. BELLINGER, *Ind. Eng. Chem. Fundamentals* **7** (1968) 576.
36. ASM International Handbook Committee (eds) "Metals Handbook", 9th Edn, Vol. 15 (ASM Int., Ohio, 1988) p. 840.

*Received 22 April
and accepted 5 August 1991*